

ARTICLE

Open Access

Strain-induced specific orbital control in a Heusler alloy-based interfacial multiferroics

Jun Okabayashi¹, Takamasa Usami^{2,3,4}, Amran Mahfudh Yatmeidhy⁵, Yuichi Murakami³, Yu Shiratsuchi^{2,4,6}, Ryoichi Nakatani^{2,4,6}, Yoshihiro Gohda^{2,5} and Kohei Hamaya^{2,3,4}

Abstract

For the development of spintronic devices, the control of magnetization by a low electric field is necessary. The microscopic origin of manipulating spins relies on the control of orbital magnetic moments (m_{orb}) by strain; this is essential for the high performance magnetoelectric (ME) effect. Herein, electric-field induced X-ray magnetic circular dichroism (XMCD) is used to determine the changes in m_{orb} by piezoelectric strain and clarify the relationship between the strain and m_{orb} in an interfacial multiferroics system with a significant ME effect; the system consists of the Heusler alloy Co_2FeSi on a ferroelectric $\text{Pb}(\text{Mg}_{1/3}\text{Nb}_{2/3})\text{O}_3\text{-PbTiO}_3$ substrate. Element-specific investigations of the orbital states by operando XMCD and the local environment via extended X-ray absorption fine structure (EXAFS) analysis show that the modulation of only the Fe sites in Co_2FeSi primarily contributes to the giant ME effect. The density functional theory calculations corroborate this finding, and the growth of the high index (422) plane in Co_2FeSi results in a giant ME effect. These findings elucidate the element-specific orbital control using reversible strain, called the 'orbital elastic effect,' and can provide guidelines for material designs with a giant ME effect.

Introduction

Combining ferromagnetic and ferroelectric properties has been investigated as multiferroics¹, which provides considerable advantages of magnetization control by an electric field (E) as a low-energy power consumption operation without electric current^{2–6}. As spintronics research pursues the suppression of power consumption for device operations, the manipulation of the spins by E is one of the solutions for future device applications^{7–12}. Recent developments have focused on the modulation of magnetization M by a low electric field strength using the benchmark of the magnetoelectric (ME) coefficient, α_E , defined as follows: $\alpha_E = \mu_0 \frac{\partial M}{\partial E}$, where μ_0 is the vacuum permeability^{13–20}. In particular, the interfaces between the

ferromagnetic and ferroelectric layers provide various options for both materials, expanding the research field of interfacial multiferroics^{2,6,10,11,21–25}.

To experimentally demonstrate material systems with large α_E values, magnetostrictive materials such as $\text{Fe}_{1-x}\text{Ga}_x$ alloys have been utilized as ferromagnetic materials^{15,16}, and piezoelectric $\text{Pb}(\text{Mg}_{1/3}\text{Nb}_{2/3})\text{O}_3\text{-PbTiO}_3$ (PMN-PT), which can introduce a strain of 0.1% by applying E ^{26–28}, has been employed as a ferroelectric material. Although a giant α_E greater than 1×10^{-5} s/m was demonstrated in epitaxial $\text{Fe}_{1-x}\text{Ga}_x/\text{PMN-PT}$ interfacial multiferroics^{15,16}, material systems compatible with spintronic technologies need to be developed^{29,30}. Recently, a study reported that $\text{Co}_2\text{FeSi}/\text{PMN-PT}$ interfacial multiferroics exhibited a large α_E of 1.8×10^{-5} s/m²⁰, where Co_2FeSi (CFS) is a Co-based Heusler alloy that was expected to have high spin polarization at room temperature and high Curie temperature^{31–35}. Other studies suggested that the origin of the large α_E value in CFS-based interfacial multiferroics was associated with strain-mediated magnetic anisotropy modulation^{36,37}.

Correspondence: Jun Okabayashi(jun@chem.s.u-tokyo.ac.jp)


¹Research Center for Spectrochemistry, The University of Tokyo, Bunkyo-ku, Tokyo 113-0033, Japan

²Center for Spintronics Research Network, Graduate School of Engineering Science, Osaka University, 1-3 Machikaneyama, Toyonaka, Osaka 560-8531, Japan

Full list of author information is available at the end of the article

These authors contributed equally: Jun Okabayashi, Takamasa Usami.

© The Author(s) 2023

 **Open Access** This article is licensed under a Creative Commons Attribution 4.0 International License, which permits use, sharing, adaptation, distribution and reproduction in any medium or format, as long as you give appropriate credit to the original author(s) and the source, provide a link to the Creative Commons license, and indicate if changes were made. The images or other third party material in this article are included in the article's Creative Commons license, unless indicated otherwise in a credit line to the material. If material is not included in the article's Creative Commons license and your intended use is not permitted by statutory regulation or exceeds the permitted use, you will need to obtain permission directly from the copyright holder. To view a copy of this license, visit <http://creativecommons.org/licenses/by/4.0/>.

The modulation of the strain-induced magnetocrystalline anisotropy energy (MAE) for CFS has thus far been discussed, whereby a relatively large MAE modulation in CFS was theoretically determined, compared with Fe₃Si, via the application of the in-plane lattice strain²⁰. However, at this moment, the microscopic origin of the giant ME effects in the CFS/PMN-PT interfacial multiferroics is still unknown.

X-ray magnetic circular dichroism (XMCD) using core-level excitation enables the detection of element-specific spin magnetic moments (m_s) and orbital magnetic moments (m_{orb}). This technique with magneto-optical sum rules has been utilized for the characterization of spintronics materials because of its precise determination of finite m_{orb} through symmetry breaking at the film interfaces. Because the changes in magnetic anisotropy are related to the anisotropic m_{orb} , the relationship between piezo strain and m_{orb} need to be explicitly clarified for interfacial multiferroic systems²⁴. Although XMCD under the application of an external E for manipulating interfacial spin has also been investigated^{38–43}, minimal research on orbital moment modulation by reversible strain has been performed^{44,45}. To initiate novel research into the physics of the relationship between the lattice distortion and orbital magnetic moments, the anisotropic m_{orb} needs to be explored even in interfacial multiferroics. Since *operando* XMCD can probe element-specific orbital modulation when a reversible strain is applied, it can be used to address a fundamental and unsolved problem in the scientific research field of novel spin and orbital physics. When we consider the relationships among m_s , m_{orb} , and strain (ϵ), the spin-orbit interaction is related to m_s and m_{orb} , and the magnetostriction is related to m_s and ϵ ²⁴. However, the relationship between m_{orb} and the lattice distortion has not been studied, even though they have conjugate relations that govern the controllability in interfacial multiferroic systems through the piezoelectric field. Therefore, the microscopic understanding between m_{orb} and ϵ is directly connected to the investigations of the giant ME effect.

In this study, we assess the microscopic origin of the giant ME effect in CFS/PMN-PT via element-specific precise measurements of the anisotropic m_{orb} and the lattice distortion by strain through *operando* spectroscopic techniques using XMCD with X-ray absorption spectroscopy (XAS) and extended X-ray absorption fine structure (EXAFS) spectroscopy. Notably, we find that the modulation of only Fe sites in Co₂FeSi predominantly contributes to the giant ME effect. The density functional theory (DFT) calculations agree with this finding, and the growth of the high-index (422) plane in Co₂FeSi causes a giant ME effect. The role of several elements, Fe and Co, can be clarified using *operando* XMCD and EXAFS; our study is the first report detecting the ‘orbital elastic effect.’

The findings from this study provide material designs for functional ME effects in interfacial multiferroics from the viewpoint of orbital states.

Results

Strain introduced into the samples

First, we describe the crystallographic orientation of the CFS layer on PMN-PT in the initial stage before introducing strain by applying E based on our previous structural characterization of CFS/PMN-PT heterostructures²⁰. Here, we used a concentration of $x = 0.3$ in $(1-x)\text{Pb}(\text{Mg}_{1/3}\text{Nb}_{2/3})\text{O}_{3-x}\text{PbTiO}_3$ because of the appearance of the large piezoelectric effect^{26,27}. The out-of-plane c -axis in PMN-PT is [011], and the in-plane [100] and [01 $\bar{1}$] directions are defined as unit cells^{26–28}. On this surface, a 10-nm-thick CFS layer with an $L2_1$ -ordered structure was grown along the out-of-plane [422] direction and in-plane [01 $\bar{1}$] and [1 $\bar{1}\bar{1}$] directions with a 0.3-nm-thick Fe buffer layer to avoid interfacial mixing^{20,46}, as illustrated in Fig. 1a. The detailed structural analyses are described in Supplemental Fig. S1. The surface was capped with a 2-nm-thick amorphous Si layer. The electrodes were mounted on the sample surface and bottom side of the PMN-PT substrate, and the voltage of the sample surface was set to ground. Since the 0.5-mm-thick PMN-PT substrates were used in this study, an applied voltage of 400 V corresponded to an electric field of 0.8 MV/m. Without an applied E , the CFS layer included a tensile strain of 0.8% with lattice matching to PMN-PT through a comparison of the bulk lattice constants, thereby resulting in the formation of an in-plane uniaxial magnetic easy axis along the [01 $\bar{1}$] direction in the CFS; this is the same as [100] in the PMN-PT orientation.

Next, under an applied E , the piezoelectric stress along the PMN-PT [100] direction could be introduced in the tensile and compressive directions using positive and negative bias voltages, respectively. The tensile [100] and compressive [01 $\bar{1}$] strains in the PMN-PT were detected²⁰. Thus, the magnetic easy axis direction in the CFS changed from the [01 $\bar{1}$] to [1 $\bar{1}\bar{1}$] direction under a negative applied E ; this change was detected by the longitudinal magneto-optical Kerr effect (MOKE), as shown in Fig. 1b. Owing to the abrupt changes in the magnetization curves caused by the magnetic field along the [01 $\bar{1}$] direction with an electric field, the domain structures in the CFS were almost completely controlled by the piezo strain. The MAE (K) was estimated to be $2.5 \times 10^4 \text{ J/m}^3$ using the area of the easy and hard axes loops. The application of a magnetic field along the orthogonal [1 $\bar{1}\bar{1}$] direction is shown in Fig. S2. The opposite behaviors of magnetic anisotropy changes were clearly observed. Furthermore, E applications were reproducibly applied for at least 20 times. This showed that the piezoelectric control along the CFS [01 $\bar{1}$] direction strongly affected the MAE modulation.

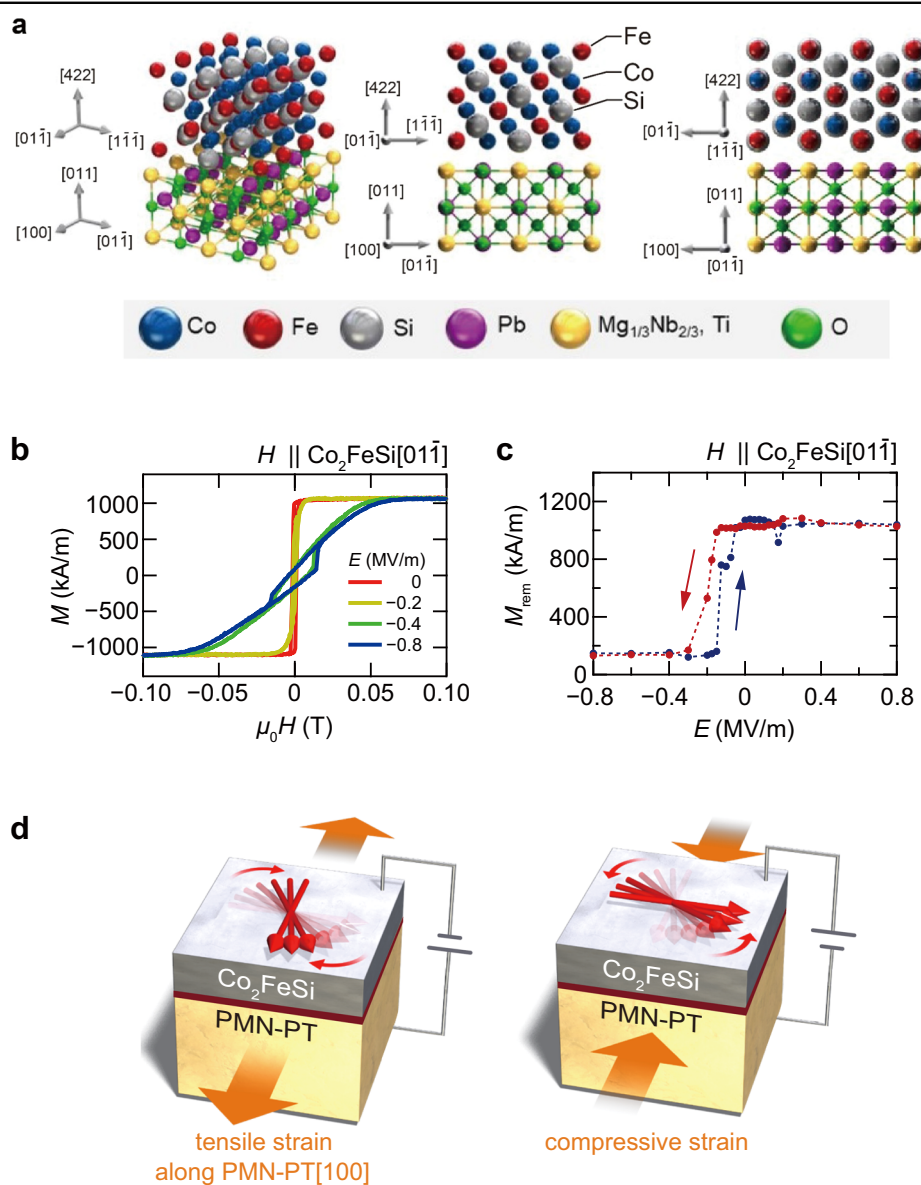


Fig. 1 Crystalline orientation at the $\text{Co}_2\text{FeSi}/\text{PMN-PT}$ interface and magnetic properties under an external electric field. **a** Crystalline orientations of CFS and PMN-PT in three-dimensional and side views from the $[01\bar{1}]$ and $[1\bar{1}\bar{1}]$ directions. **b** Magnetization curves estimated from the magneto-optic Kerr effect measurement under an applied electric field (E) when a magnetic field (H) is applied along the in-plane PMN-PT $[100]$ direction. **c** E dependence of the estimated remanent magnetization (M_{rem}). **d** Schematic illustrations of the changes in the magnetic anisotropy by an applied E in the strain directions.

Operando XAS and XMCD

Figure 2 shows the Fe and Co L -edge XAS and XMCD spectra obtained in the partial fluorescence yield (PFY) mode under an applied electric field E of ± 0.8 MV/m. The sample surfaces were connected to the ground, and E was applied to the back side of the PMN-PT substrates. Note that the PFY mode probed depth information approximately 10 nm beneath the surface because of the photon-in and photon-out processes⁴⁷. In addition, total-electron-yield (TEY) mode, which measures the drain

currents and detects signals of 3 nm from the sample surface, was used to analyze the XAS and XMCD line shapes without an applied E . The XAS spectral line shapes shown in Fig. 2a, b originated from metallic Fe and Co features in CFS. In particular, the satellite structures in Co XAS appeared in the cases of highly ordered Co-based Heusler alloys^{48–51}. The spectral line shapes of XMCD and the slight change in the L_3 -edge peak were modulated by E only at the Fe L -edge, despite the fixed sample measurement position. A comparison of the results for

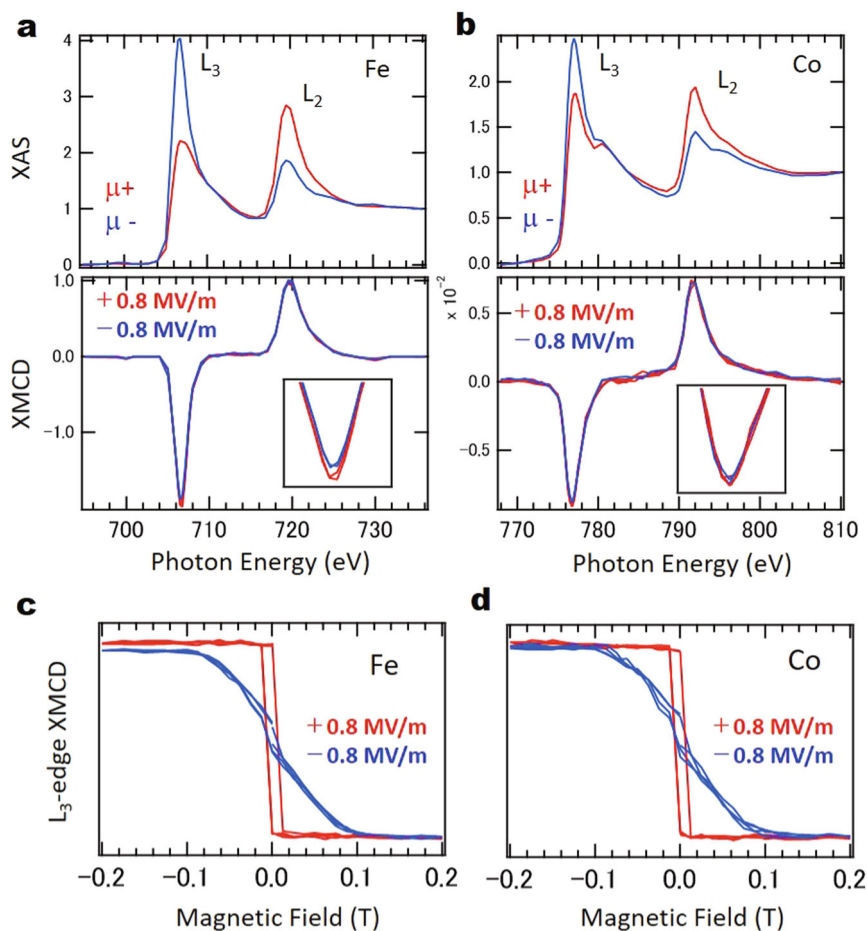


Fig. 2 XAS and XMCD under an applied electric field in Co₂FeSi/PMN-PT. **a** Fe and **b** Co *L*-edges at ±0.8 MV/m. Expanded views around *L*₃ edges are shown in the bottom panels. Four measurements are repeatedly displayed by plus and minus electric fields. Insets show the expanded views near the *L*₃-edge XMCD. Magnetic field dependence of *L*₃-edge XMCD under an applied electric field. **c** Fe and **d** Co *L*-edges at ±0.8 MV/m. Four measurements are displayed repeatedly by plus and minus electric fields. In **(c)**, positive and negative electric field cases are aligned in the positive magnetic field region to emphasize the difference in the negative magnetic field side.

positive and negative E showed a slight variation in the peak asymmetries between the L_3 - and L_2 -edges. Since the convergent values of the integrals of the XMCD are proportional to m_{orb} within the framework of the XMCD sum rule^{52–54}, these results indicated that the m_{orb} were modulated by the applied E , thereby resulting in changes in magnetic anisotropy⁵⁵. The values of m_s and m_{orb} in Fe were estimated to be 1.84 and 0.176 μ_B from the spectra recorded in TEY mode, corresponding to the case of +0.8 MV/m electric field. Details are described in Fig. S3. For an electric field of -0.8 MV/m, the changes at the L_3 -edge in the PFY mode contributed to the integral of XMCD. The modulation of m_{orb} by 0.01 μ_B under an applied E was related to the induced lattice distortion from the PMN-PT substrates. Moreover, after releasing E to zero, the spectral line shapes reverted to those of the pristine state. The modulation of m_s was less than 0.01 μ_B despite being one order larger m_s than m_{orb} . Evidently, m_s

did not contribute to the MAE in the case of the CFS (422) orientation, and the effect of the magnetic dipole term m_T was negligible. In contrast to the case of Fe, no spectral changes were detected for the case of the Co L -edge XMCD. The m_s and m_{orb} values at the Co sites were estimated to be 0.60 and 0.131 μ_B , respectively. These results indicated that orbital moment anisotropy in Fe was essential, whereas that in Co remained unchanged. Therefore, these results were caused by the modulation of the orbital moments rather than the spin moments, thus indicating that the inverse magnetostriction effects, which are discussed as macroscopic phenomena, were derived from the changes in m_{orb} from the viewpoint of electronic structures.

The element-specific XMCD hysteresis curves (M - H curves) at the Fe and Co L_3 -edges during the application of E in the oblique-incidence setup are also shown in Fig. 2c, d. In the case of +8 MV/m, easy axis behavior was

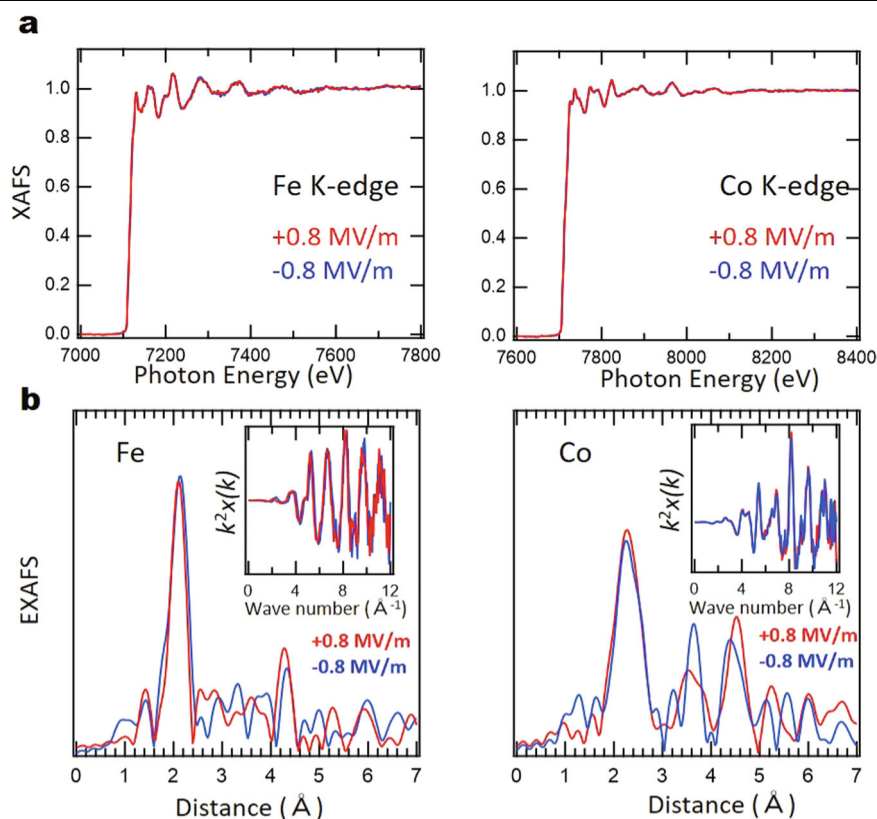


Fig. 3 XAFS and EXAFS analysis under an applied electric field in $\text{Co}_2\text{FeSi/PMN-PT}$. **a** XAFS spectra of Fe and Co K -edges under ± 0.8 MV/m. **b** EXAFS analysis through the Fourier transform of the XAFS oscillation shown in the insets.

clearly observed, whereas the -0.8 MV/m case indicated the hard axis. The measurements were repeatedly performed four times in the $+, -, +, -$ sequence under the fixed conditions of incident beam helicity and sample position. This result showed reproducible behavior of the changes in the magnetic easy-axis direction. In the case of Fe shown in Fig. 2c, the vertical axis strength was slightly different between ± 0.8 MV/m, thus affecting the changes in XMCD in the Fe L_{3-} edge intensity, whereas the M - H curves of Co by ± 0.8 MV/m overlapped above the saturation magnetic fields (Fig. 2d). Therefore, only the change in m_{orb} for Fe was experimentally found. In addition, the changes in the easy axis direction were similar for both Fe and Co because of the exchange coupling between these sites.

Operando EXAFS

To further explore the local environment around the Fe and Co atoms, XAFS measurements with EXAFS analysis of the Fe and Co K -edges during the application of E were performed to deduce the changes in the nearest-neighbor distance using a Fourier transform. As shown in Fig. 3a, the Fe and Co K -edge absorption spectra with EXAFS oscillatory behaviors are observed in the fluorescence yield

mode. Clear XAFS oscillations are detected and plotted at wavenumber k in the inset of Fig. 3b. The XAFS oscillation function $k^2\chi(k)$ can be fitted by the FEFF8 program⁵⁶. The Fourier transformed EXAFS profile for the real-space view of the local structure is displayed in Fig. 3b and considers the information up to the second-nearest neighbor sites and using the range of $k = 3 - 13 \text{ \AA}^{-1}$. Owing to the effect of the phase shift, the peak position in the EXAFS was not directly related to the bond length. Using the fitting procedure shown in the Supplemental Information, the nearest bond lengths in both Fe and Co sites are estimated to be 2.22 and 2.33 \AA , respectively, for the $+0.8$ MV/m case; these values are almost identical to the bulk CFS^{57,58}. The linearly polarized incident beam is used to detect the absorption along the $[011]$ direction in the CFS. Under a negative applied E on the PMN-PT substrate as a compressive strain, the nearest neighbor distances in the Fe and Co sites change -0.27% and 0.09% , respectively; these potentially originate from the orientation of the CFS layer in the high-index (422) plane. These element-specific distortions could not be detected by X-ray diffraction in the 10-nm-thick CFS films. These findings indicated that the tensile local distortion in Fe triggered a change in m_{orb} in the CFS layer.

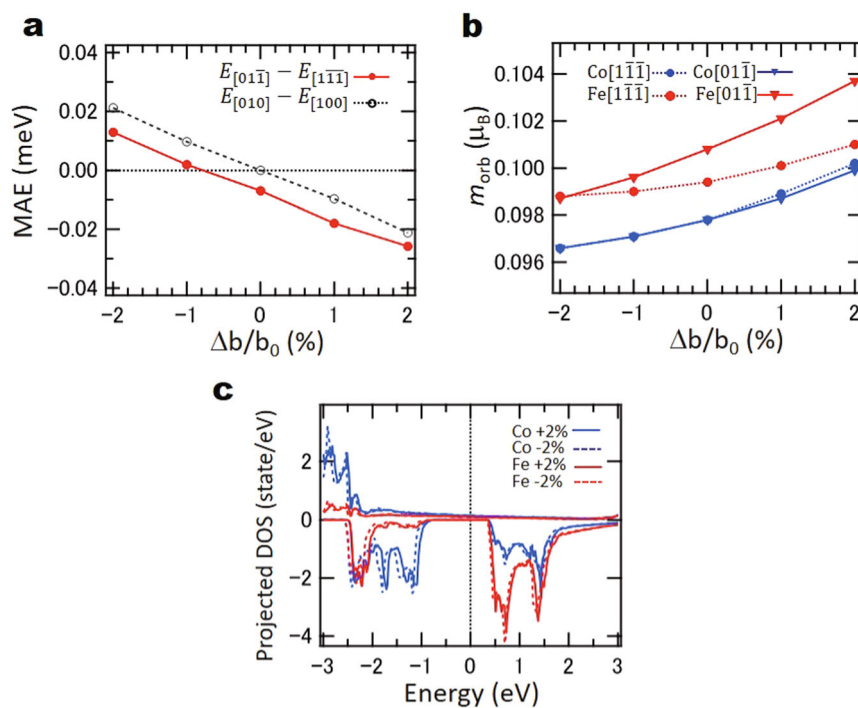


Fig. 4 Strain-induced magnetic anisotropy energy, orbital magnetic moments, and density of states by DFT calculation in Co_2FeSi . **a** Total energy differences along the in-plane across two axial directions in the (422) and (001) orientations depending on the b -axis strain ($\Delta b/b_0$). **b** Element-specific orbital magnetic moments along two axis directions in the (422) orientation. **c** Element-specific density of states depending on the strain for the (422) orientation.

DFT calculations

The spin- and orbital-resolved electronic structures were examined using first-principles DFT calculations and depended on the film orientation and strain. Since the CFS layers were deposited along the CFS [422] c -axis direction on PMN-PT (011), the same unit cell structures as in the experimental situations were employed. The in-plane b -axis and other orthogonal axes were defined as the $[01\bar{1}]$ and $[1\bar{1}\bar{1}]$ directions of the CFS layer, respectively. In a previous report, the strain dependence of the band structures along the $[001]$ direction was also investigated, along with the highly symmetric $[100]$ and $[010]$ directions²⁰. Here, the strain dependence of the MAE on the b -axis and $\Delta b/b_0$ in terms of the equilibrium cubic structure are displayed in Fig. 4a. The CFS layer grown on PMN-PT was strained by +0.8% along the $[01\bar{1}]$ b -axis direction at the initial stage. The lattice parameters along the other directions were relaxed to minimize structural formation energies. MAE is defined as the in-plane total energy difference ($E[01\bar{1}] - E[1\bar{1}\bar{1}]$). The changes in the easy axis were observed by the b -axis strain. However, the modulation of the easy-hard axis that occurred with the strain was different from the experimental results because the effective experimental strain was difficult to estimate. For the MAE in the highly

symmetric case between the $[100]$ and $[010]$ directions, the strain was relaxed completely in the bulk form. To elucidate the changes in magnetic anisotropy, the values of m_{orb} , depending on the strain, were estimated, as shown in Fig. 4b. Evidently, a large modulation was observed in the case of $m_{orb}(\epsilon)$ along the Fe $[01\bar{1}]$ direction; this result was comparable to the XMCD results. The slope of $m_{orb}(\epsilon)$ depending on the strain differed between the Fe $[01\bar{1}]$ and $[1\bar{1}\bar{1}]$ directions, and the strong dependence of Fe $[01\bar{1}]$ m_{orb} led to orbital control by the Fe sites with the application of b -axis strain, indicating a linear relationship between the difference in $m_{orb}(\epsilon)$ and MAE. In contrast, in the case of the Co sites, similar tendencies were displayed for all directions, thus indicating a cubic local environment. Furthermore, its strain dependence of m_{orb} in the cases of $[100]$ and $[010]$ was also plotted, and the tendency was low compared with that of the Fe $[01\bar{1}]$ case (see Supplemental Information). Therefore, the giant ME effects in CFS/PMN-PT(011) relied on high-index (422) growth and the modulation of m_{orb} along $[01\bar{1}]$ by strain. To further analyze the orbital states, the dependence of the element-specific density of states (DOS) on the orientation and strain was examined, as shown in Fig. 4c. In the cases of $\pm 2\%$ strain, the projected DOS exhibited half-metallic properties, with

the energy gap in the minority spin states using the intra-Coulomb repulsion energy using the DFT + U method. Since m_{orb} originated from the spin-conserved band transition in the scheme of second-order perturbation for spin-orbit interaction, the changes in DOS by strain slightly affected $m_{\text{orb}}(\epsilon)$. The unoccupied DOS in the Fe $3d$ state was modulated by the strain, which primarily corresponded to the modulation of $m_{\text{orb}}[01\bar{1}]$.

Discussion

First, we discuss the physical meaning of $m_{\text{orb}}(\epsilon)$ obtained from XMCD and DFT calculations. The changes in magnetic anisotropy originated from the anisotropic m_{orb} and are calculated by $\Delta m_{\text{orb}} = m_{\text{orb}}([01\bar{1}]; 0 \text{ MV/m}) - m_{\text{orb}}([01\bar{1}]; -0.8 \text{ MV/m})$; this corresponds to the orbital elastic anisotropy. The DFT calculations found four cases of m_{orb} ($[01\bar{1}]$, $[1\bar{1}1]$; equilibrium) and m_{orb} ($[01\bar{1}]$, $[1\bar{1}1]$; strained). The differences by strain are comparable to the E -induced XMCD and are defined as $\Delta m_{\text{orb}}(\epsilon)$ (the difference between $m_{\text{orb}}([01\bar{1}]; \text{equilibrium})$ and $m_{\text{orb}}([01\bar{1}]; \text{strained})$). Notably, according to anisotropic orbital moment theory, the magnetic anisotropy energy $K = 1/4 \xi \alpha \Delta m_{\text{orb}}(\epsilon)$ can be applied using the perturbation of the spin-orbit interaction $\xi_{\text{Fe}} = 50 \text{ meV}$. Furthermore, α of 0.2 is a constant that depends on the band structure, and this is applicable for metallic Fe^{59,60}. Using these parameters and the unit cell volume of CFS, the value of K in the Fe sites is estimated to be $1.1 \times 10^5 \text{ J/m}^3$ by strain; this value is comparable to that of $K = 2.5 \times 10^4 \text{ J/m}^3$ from the magnetization measurements. The values of m_s , m_{orb} , and MAE are listed in Table 1. In the case of the Co sites, since $\Delta m_{\text{orb}}(\epsilon) = 0$, no contributions to the MAE were observed. Compared with the DFT calculation, the difference originated from the disordering in the CFS layer because the calculation was performed in a perfectly ordered $L2_1$ structure. In the case of the CFS layer grown at relatively low temperatures, $D0_3$ -type disordering was introduced⁶¹, which could suppress the magnetic moment values. However, because the DFT calculation did not include Hund's second rule, that is, a relativistic effect is

not explicitly included, the values of m_{orb} were underestimated. The value of m_s in Fe estimated by the calculations was larger than that in bulk Fe ($2.3 \mu_B$), thus indicating electron localization in the Fe $3d$ states. Note that the MAE values estimated from the orbital moment anisotropy are generally one order of magnitude larger than those obtained from the magnetization measurements. Therefore, the changes in anisotropy due to E can be explained by the modulation of m_{orb} . These phenomena indicate a novel orbital control through the elastic effect, where the macroscopic magnetoelastic effect can be interpreted from the viewpoint of electronic structures.

Next, the reasons for the m_{orb} changes reliance only on the Fe sites are discussed. In Co-based Heusler alloy compounds, the DOS of Co is generally dominant at E_F for half-metallic conductivity, as shown in Fig. 4c; however, the DOS of Fe is located deep in the valence band and thus contributes to the local magnetic moments. Herein, an analogous property of B -site localization in Heusler alloy A_2BX is also discussed in the Mn sites of Co_2MnSi , considering U for the B -sites⁶². The Fe sites are relatively localized and contribute to the orbital polarization and formation of m_{orb} , and the Co sites are dominant for the highly spin-polarized transport properties. The nonmagnetic element X can be valid for structural stability and tuning of the energy band gap and the position of the Fermi level. The role of each element is relevant in the CFS layer and can be tuned by strain. Therefore, the control of the m_{orb} only in Fe with an applied strain is plausible for the MAE control in Co-based Heusler alloy compounds. These element-specific analyses can be achieved only by *operando* XMCD.

Third, although magnetostriction or magnetoelastic effects have been recognized as strain effects in magnetism as phenomenologically macroscopic understanding for some materials, a microscopic understanding of the electronic structures and orbital states is lacking. Recent studies on ultrathin ferromagnetic films need to include a more detailed analysis of the restrictive effects at the interfaces. A novel concept of orbital strictive or orbital elastic effects is a potential candidate. The strain-dependent orbital magnetic moments are formulated as a linear relationship, as follows: $m_{\text{orb}}(\epsilon) = m_{\text{orb}}^0 (1 + \lambda \epsilon)$, where m_{orb}^0 is the equilibrium constant and λ is the coefficient. The linear relationship is obtained from the enhancement of m_{orb} in the spin-conserved electron motion in the in-plane direction at the interfaces. The magnetostriction constant for CFS is estimated to be 12.22×10^{-6} ⁶³, and this value is comparable with our definition of the orbital-strictive coefficient λ . Since the direction of the applied strain and the enhancement of m_{orb} were the same along the b -axis, the strain along the other directions was low. These phenomena were significant for the high-index (422) plane in the CFS (422)/PMN-PT (011) system.

Table 1 Element-specific m_s and m_{orb} and anisotropic m_{orb} by strain (Δm_{orb}) estimated from XMCD and DFT calculations.

	Fe		Co	
	XMCD	DFT	XMCD	DFT
m_s [μ_B]	1.836	3.52	0.603	1.48
m_{orb} [μ_B]	0.176	0.101	0.131	0.098
Δm_{orb} [μ_B]	0.01	–	0	–
MAE [meV]	0.03	–	0	–

Finally, we discuss the enhancement of the ME effect in the CFS/PMN-PT interface. Regarding the crystalline orientation, the growth of the CFS along the [422] direction can be energetically stabilized in the PMN-PT (011) case compared with the PMN-PT (001) orientation. The strain in the CFS (422) plane triggers the modulation of the lattice constants in the highly symmetric [100], [010], and [001] directions, thereby resulting in the modulation of m_{orb} in Fe. Therefore, the elemental selectivity and crystalline orientation are indispensable for designing materials with large ME effects.

In conclusion, we developed E -induced XMCD to detect the changes in m_{orb} by the piezoelectric strain and clarified the relationship between the strain and m_{orb} in an interfacial multiferroic system with a giant ME effect; the system consisted of the Heusler alloy CFS on a ferroelectric PMN-PT substrate. Element-specific investigations of the orbital states by operando XMCD and the local environment by EXAFS analysis showed that the modulation of only the Fe sites in CFS contributed to the giant ME effect. The DFT calculations agreed this finding, and the growth in the high-index (422) plane in the CFS resulted in a giant ME effect. Our findings resulted from the element-specific orbital control by reversible strain recognized as the ‘orbital elastic effect’ and could provide guidelines for material designs with a giant ME effect using orbital-elastic highly spin-polarized Heusler alloys to advance interfacial multiferroics.

Method

Sample growth

The samples were grown using ultrahigh-vacuum molecular beam epitaxy on [011]-oriented 0.5-mm-thick PMN-PT single-crystal substrates. Therefore, a bias voltage of ± 400 V applied between the top and bottom electrodes resulted in an electric field of ± 0.8 MV/m. Before the deposition of a 10-nm-thick CFS layer, a 0.3-nm-thick Fe layer was deposited onto the substrate at 300 °C. The flat surfaces of the PMN-PT substrates were prepared by annealing at 400 °C for 20 min. The CFS layer was grown at 300 °C and covered with 2-nm-thick Si to prevent oxidation at room temperature. The details of the surface and interface conditions and fabrication procedures are reported in ref. 20. The magnetic properties were characterized using longitudinal MOKE measurements under an applied E and magnetometry using a vibrating-sample magnetometer (VSM). The magnetization values were estimated from the VSM. The changes in M - H curves under an applied E were monitored by MOKE.

XMCD and EXAFS

XAS and XMCD measurements of the Fe and Co L -edges were performed using the High-Energy Accelerator Research Organization, Photon Factory (KEK-PF) BL-7A beamline, Japan, at room temperature. A magnetic field of

± 0.2 T was applied along the incident polarized soft X-rays to sufficiently saturate the magnetization along the normal direction of the surface of the sample. TEY mode was used to detect the drain currents from the samples for measurements recorded without the application of a magnetic field. The electrodes were mounted on the surface of the sample and the rear of the substrate to perform the E -induced XMCD measurements. E -induced XMCD measurements were performed using the PFY mode to probe signals 10 nm below the surfaces of the samples using a bipolar electric power source (Keithley 2410) to apply E to PMN-PT. The fluorescence signals were detected using a silicon drift detector (Princeton Gamma-Tech. Instrument Inc., SD10129) and mounted 90° to the incident beam. The XAS and XMCD measurements were performed in an oblique incidence setup of 60° from the normal of the sample surface from the incident beam and magnetic field, and the signals of the in-plane components in the films were detected. We changed the magnetic field directions to obtain right- and left-hand polarized X-rays while fixing the polarization direction of the incident X-rays. To avoid the saturation effects in PFY mode, the intensities of the XAS measurements were carefully examined by their comparison with those obtained in TEY mode.

The EXAFS measurements at the Fe and Co K edge under an applied E were performed at BL-12C at KEK-PF using the fluorescence yield mode with a 19-element solid-state detector at room temperature. A linearly polarized incident beam arrived at the sample from the 45° direction and enabled the detection of the signals along the $[01\bar{1}]$ direction. The system that applied the E was the same as that employed in E -induced XMCD.

Computational details in DFT calculations

First-principle calculations were performed based on DFT using the OpenMX code⁶⁴. The generalized gradient approximation was used with the PBE exchange-correlation functional⁶⁵. In addition, the DFT + U method with effective Hubbard repulsion $U_{\text{eff}} = 2.6$ eV and $U_{\text{eff}} = 2.5$ eV was employed for the Co 3d and Fe 3d orbitals of Co₂FeSi, respectively. The k -point grids were set to $15 \times 15 \times 15$ and $11 \times 13 \times 15$ for CFS (001) and CFS (422), respectively. The in-plane strain was generated by changing the in-plane lattice parameters a and b in the CFS (422) layer. Here, the strain was approximated by $\Delta a/a_0$ and $\Delta b/b_0$, where $\Delta a = a - a_0$, $\Delta b = b - b_0$. For CFS (001), a_0 ($= b_0$) was the equilibrium lattice constant without strain. For the CFS (422), b_0 was set to the equilibrium CFS lattice parameters. The MAE was evaluated as the total energy difference obtained from the calculations, including the spin-orbit coupling for the magnetization fully self-consistently along the [100] and [010] directions.

Acknowledgements

This work was partially supported by JST CREST, Grant Number JPMJCR18J1; JSPS KAKENHI, Grant Numbers JP19H05616, JP21K14196, JP22H04966, and JP22H05000; the Spintronics Research Network of Japan (Spin-RNJ), and Yazaki Memorial Foundation for Science and Technology. Some calculations were performed using supercomputers at the ISSP, University of Tokyo, and TSUBAME, Tokyo Institute of Technology. Some of the synchrotron radiation experiments were performed with the approval of the Photon Factory Program Advisory Committee, KEK (No. 2021G069).

Author details

¹Research Center for Spectrochemistry, The University of Tokyo, Bunkyo-ku, Tokyo 113-0033, Japan. ²Center for Spintronics Research Network, Graduate School of Engineering Science, Osaka University, 1-3 Machikaneyama, Toyonaka, Osaka 560-8531, Japan. ³Department of Systems Innovation, Graduate School of Engineering Science, Osaka University, 1-3 Machikaneyama, Toyonaka, Osaka 560-8531, Japan. ⁴Spintronics Research Network Division, Institute for Open and Transdisciplinary Research Initiatives, Osaka University, 2-1 Yamadaoka, Suita, Osaka 565-0871, Japan. ⁵Department of Materials Science and Engineering, Tokyo Institute of Technology, Nagatsuta-cho 4259, Midori-ku, Yokohama 226-8502, Japan. ⁶Division of Materials and Manufacturing Science, Graduate School of Engineering, Osaka University, 2-1 Yamadaoka, Suita 565-0871 Osaka, Japan

Author contributions

J.O. and K.H. conducted the study. T.U. prepared the samples and characterized their properties with the help of Y.M., Y.S., and R.N. J.O. set up the operando XMCD and EXAFS measurement apparatus at the Photon Factory and collected and analyzed the data with the help of T.U. A.M.Y. and Y.G. performed first-principles calculations. J.O. prepared the manuscript using inputs from the coauthors. All the authors discussed the results and wrote the manuscript.

Competing interests

The authors declare no competing interests.

Publisher's note

Springer Nature remains neutral with regard to jurisdictional claims in published maps and institutional affiliations.

Supplementary information The online version contains supplementary material available at <https://doi.org/10.1038/s41427-023-00524-6>.

Received: 1 September 2023 Revised: 9 November 2023 Accepted: 24 November 2023

Published online: 10 January 2024

References

- Schmid, H. Multi-ferroic magnetoelectrics. *Ferroelectrics* **162**, 317–338 (1994).
- Spaldin, N. A. & Ramesh, R. Advances in magnetoelectric multiferroics. *Nat. Mater.* **18**, 203–212 (2019).
- Hu, J.-M., Duan, C.-G., Nan, C.-W. & Chen, L.-Q. Understanding and designing magneto-electric heterostructures guided by computation: progresses, remaining questions, and perspectives. *npj Comput. Mater.* **3**, 18 (2017).
- Hu, J. M., Li, Z., Chen, L. Q. & Nan, C. W. High-density magnetoresistive random access memory operating at ultralow voltage at room temperature. *Nat. Commun.* **2**, 553 (2011).
- Manipatruni, S. et al. Scalable energy-efficient magnetoelectric spin-orbit logic. *Nature* **565**, 35–42 (2019).
- Hu, J.-M. & Nan, C.-W. Opportunities and challenges for magnetoelectric devices. *APL Mater.* **7**, 080905 (2019).
- Matsukura, F., Tokura, Y. & Ohno, H. Control of magnetism by electric fields. *Nat. Nanotechnol.* **10**, 209220 (2015).
- Chiba, D. et al. Magnetization vector manipulation by electric fields. *Nature* **455**, 515–518 (2008).
- Maryama, T. et al. Large voltage-induced magnetic anisotropy change in a few atomic layers of iron. *Nat. Nanotechnol.* **4**, 158–161 (2009).
- Taniyama, T. Electric-field control of magnetism via strain transfer across ferromagnetic/ferroelectric interfaces. *J. Phys: Condens. Matter* **27**, 504001 (2015).
- Vaz, C. A. Electric field control of magnetism in multiferroic heterostructures. *J. Phys: Condens. Matter* **24**, 333201 (2012).
- Shiratsuchi, Y., Toyoki, K. & Nakatani, R. Magnetoelectric control of anti-ferromagnetic domain state in Cr₂O₃ thin film. *J. Phys: Condens. Matter* **33**, 243001 (2021).
- Zhang, S. et al. Giant electrical modulation of magnetization in Co₄₀Fe₄₀B₂₀/Pb(Mg_{1/3}Nb_{2/3})_{0.7}Ti_{0.3}O₃(011) heterostructure. *Sci. Rep.* **4**, 3727 (2014).
- Wang, J. et al. Giant non-volatile magnetoelectric effects via growth anisotropy in Co₄₀Fe₄₀B₂₀ films on PMN-PT substrates. *Appl. Phys. Lett.* **114**, 092401 (2019).
- Meisenheimer, P. B. et al. Engineering new limits to magnetostriction through metastability in iron-gallium alloys. *Nat. Commun.* **12**, 2757 (2021).
- Begue, A. & Ciria, M. Strain-mediated giant magnetoelectric coupling in a crystalline multiferroic heterostructure. *ACS Appl. Mater. Interfaces* **13**, 6778–6784 (2021).
- Zhang, S. et al. Electric-field control of nonvolatile magnetization in Co₄₀Fe₄₀B₂₀/Pb(Mg_{1/3}Nb_{2/3})_{0.7}Ti_{0.3}O₃ structure at room temperature. *Phys. Rev. Lett.* **108**, 137203 (2012).
- Ghidini, M. et al. Shear-strain-mediated magnetoelectric effects revealed by imaging. *Nat. Mater.* **18**, 840–845 (2019).
- Ba, Y. et al. Electric-field control of skyrmions in multiferroic heterostructure via magnetoelectric coupling. *Nat. Commun.* **12**, 322 (2021).
- Fujii, S. et al. Giant converse magnetoelectric effect in a multiferroic heterostructure with polycrystalline Co₂FeSi. *NPG Asia Mater.* **14**, 43 (2022).
- Venkataiah, G., Shirahata, Y., Itoh, M. & Taniyama, T. Manipulation of magnetic coercivity of Fe film in Fe/BaTiO₃ heterostructure by electric field. *Appl. Phys. Lett.* **99**, 102506 (2011).
- Radaelli, G. et al. Electric control of magnetism at the Fe/BaTiO₃ interface. *Nat. Commun.* **5**, 3404 (2014).
- Shirahata, Y. et al. Electric-field switching of perpendicularly magnetized multilayers. *NPG Asia Mater.* **7**, e198–e198 (2015).
- Okabayashi, J., Miura, Y. & Taniyama, T. Strain-induced reversible manipulation of orbital magnetic moments in Ni/Cu multilayers on ferroelectric BaTiO₃. *npj Quantum Mater.* **4**, 21 (2019).
- Sahoo, S. et al. Ferroelectric control of magnetism in BaTiO₃/Fe heterostructures via interface strain coupling. *Phys. Rev. B* **76**, 092108 (2007).
- Park, S.-E. & Shrout, T. R. Ultrahigh strain and piezoelectric behavior in relaxor based ferroelectric single crystals. *J. Appl. Phys.* **82**, 1804–1811 (1997).
- Noheda, B., Cox, D. E., Shirane, G., Gao, J. & Ye, Z. G. Phase diagram of the ferroelectric relaxor (1-x)PbMg_{1/3}Nb_{2/3}O₃-xPbTiO₃. *Phys. Rev. B* **66**, 054104 (2002).
- Baek, S. H. et al. Giant piezoelectricity on Si for hyperactive MEMS. *Science* **334**, 958–961 (2011).
- Yang, Y. et al. Controlling the anomalous Hall effect by electric-field-induced piezo-strain in Fe₄₀Pt₆₀/(001)-Pb(Mg_{1/3}Nb_{2/3})_{0.67}Ti_{0.33}O₃ multiferroic heterostructures. *Appl. Phys. Lett.* **112**, 033506 (2018).
- Yang, Y. et al. Electric-field-assisted non-volatile magnetic switching in a magnetoelectronic hybrid structure. *iScience* **24**, 102734 (2021).
- Hamaya, K. et al. Estimation of the spin polarization for Heusler-compound thin films by means of nonlocal spin-valve measurements: Comparison of Co₂FeSi and Fe₃Si. *Phys. Rev. B* **85**, 100404(R) (2012).
- Hamaya, K. & Yamada, M. Semiconductor spintronics with Co₂-Heusler compounds. *MRS Bull.* **47**, 584–592 (2022).
- Wurmehl, S. et al. Geometric, electronic, and magnetic structure of Co₂FeSi: Curie temperature and magnetic moment measurements and calculations. *Phys. Rev. B* **72**, 184434 (2005).
- Kimura, T., Hashimoto, N., Yamada, S., Miyao, M. & Hamaya, K. Room-temperature generation of giant pure spin currents using epitaxial Co₂FeSi spin injectors. *NPG Asia Mater.* **4**, e9 (2012).
- Okabayashi, J. Element-specific spin states in heusler-alloy compounds probed by X-ray magnetic spectroscopy, progress in photon science, springer series in chemical physics **125**, p. 169 (Springer Nature Switzerland AG, 2021)
- Usami, T. et al. Giant magnetoelectric effect in an L₂₁-ordered Co₂FeSi/Pb(Mg_{1/3}Nb_{2/3})_{0.7}Ti_{0.3}O₃ multiferroic heterostructure. *Appl. Phys. Lett.* **118**, 142402 (2021).
- Yamada, S. et al. Electric field tunable anisotropic magnetoresistance effect in an epitaxial Co₂FeSi/BaTiO₃ interfacial multiferroic system. *Phys. Rev. Mater.* **5**, 014412 (2021).

38. Miwa, S. et al. Voltage-controlled magnetic anisotropy in Fe|MgO tunnel junctions studied by x-ray absorption spectroscopy. *Appl. Phys. Lett.* **107**, 162402 (2015).
39. Bi, C. et al. Reversible control of Co magnetism by voltage-induced oxidation. *Phys. Rev. Lett.* **113**, 267202 (2014).
40. Zhang, B. et al. Electric-field-induced strain effects on the magnetization of a $\text{Pr}_{0.67}\text{Sr}_{0.33}\text{MnO}_3$ film. *Phys. Rev. B* **91**, 174431 (2015).
41. Welke, M. et al. XMCD studies of thin Co films on BaTiO_3 . *J. Phys: Condens. Matter* **27**, 326001 (2015).
42. Hoffmann, M. et al. Study of electronic and magnetic properties and related x-ray absorption spectroscopy of ultrathin Co films on BaTiO_3 . *J. Phys: Condens. Matter* **27**, 426003 (2015).
43. Amemiya, K. & Sakamaki, M. Voltage-induced changes in magnetism of $\text{FeCo}/\text{BaTiO}_3$ thin films studied by X-ray absorption spectroscopy. *e-J. Surf. Sci. Nanotechnol.* **13**, 465–468 (2015).
44. Zhang, Z. et al. Strain-controlled spin wave excitation and gilbert damping in flexible Co_2FeSi films activated by femtosecond laser pulse. *Adv. Funct. Mater.* **31**, 2007211 (2021).
45. Zhao, Z. et al. X-ray magnetic circular dichroism investigation of electric field manipulation of magnetization reversal in $\text{Ta}/\text{CoFeB}/(011)\text{PMN-PT}$ heterostructure. *Appl. Phys. Express* **13**, 013002 (2020).
46. Zheng, M., Usami, T. & Taniyama, T. Shear-strain-mediated large nonvolatile tuning of ferromagnetic resonance by an electric field in multiferroic heterostructures. *NPG Asia Mater.* **13**, 7 (2021).
47. Stöhr, J. & Siegmann, H. C. *Magnetism from Fundamentals to Nanoscale Dynamics* (Springer Berlin Heidelberg, 2006).
48. Meinert, M. et al. Insights into the electronic structure of Co_2FeSi from x-ray magnetic linear dichroism. *Phys. Rev. B* **86**, 054420 (2012).
49. Kallmayer, M. et al. Spin-resolved unoccupied density of states in epitaxial Heusler-alloy films. *Phys. Rev. B* **80**, 020406 (2009).
50. Okabayashi, J., Sukegawa, H., Wen, Z., Inomata, K. & Mitani, S. Large anisotropic Fe orbital moments in perpendicularly magnetized Co_2FeAl Heusler alloy thin films revealed by angular-dependent x-ray magnetic circular dichroism. *Appl. Phys. Lett.* **103**, 102402 (2013).
51. Wen, Z. et al. Interdiffusion in epitaxial ultrathin $\text{Co}_2\text{FeAl}/\text{MgO}$ heterostructures with interface-induced perpendicular magnetic anisotropy. *Appl. Phys. Express* **10**, 013003 (2017).
52. Chen, C. T. et al. Experimental confirmation of the X-ray magnetic circular dichroism sum rules for iron and cobalt. *Phys. Rev. Lett.* **75**, 152–155 (1995).
53. van der Laan, G. & Figuera, A. I. X-ray magnetic circular dichroism—A versatile tool to study magnetism. *Coord. Chem. Rev.* **277–278**, 95–129 (2014).
54. Okabayashi, J. in *Progress in Photon Science: Recent Advances* (Eds. Yamamoto, K., Tunik, S. & Makarov, V.) 471–492 (Springer International Publishing, 2019).
55. Miura, Y. & Okabayashi, J. Understanding magnetocrystalline anisotropy based on orbital and quadrupole moments. *J. Phys: Condens. Matter* **34**, 473001 (2022).
56. Ankudinov, A. L., Ravel, B., Rehr, J. J. & Conradson, S. D. Real-space multiple-scattering calculation and interpretation of x-ray-absorption near-edge structure. *Phys. Rev. B* **58**, 7565–7576 (1998).
57. Karel, J. et al. Influence of nanoscale order–disorder transitions on the magnetic properties of Heusler compounds for spintronics. *J. Mater. Chem. C* **5**, 4388–4392 (2017).
58. Balke, B. et al. Structural characterization of the Co_2FeZ ($Z=\text{Al}, \text{Si}, \text{Ga}, \text{and Ge}$) Heusler compounds by x-ray diffraction and extended x-ray absorption fine structure spectroscopy. *Appl. Phys. Lett.* **90**, 172501 (2007).
59. Okabayashi, J. et al. Perpendicular magnetic anisotropy at the $\text{Fe}/\text{Au}(111)$ interface studied by Mössbauer, x-ray absorption, and photoemission spectroscopies. *Phys. Rev. B* **103**, 104435 (2021).
60. Wilhelm, F. et al. Magnetic anisotropy energy and the anisotropy of the orbital moment of Ni in Ni/Pt multilayers. *Phys. Rev. B* **61**, 8647–8650 (2000).
61. Kudo, K. et al. Great differences between low-temperature grown Co_2FeSi and Co_2MnSi films on single-crystalline oxides. *ACS Appl. Electron. Mater.* **1**, 2371–2379 (2019).
62. Nawa, K. & Miura, Y. Exploring half-metallic Co-based full Heusler alloys using a DFT + U method combined with linear response approach. *RSC Adv.* **9**, 30462–30478 (2019).
63. Pandey, H. et al. Magnetoelastic coupling induced magnetic anisotropy in $\text{Co}_2(\text{Fe}/\text{Mn})\text{Si}$ thin films. *Appl. Phys. Lett.* **104**, 022402 (2014).
64. Ozaki, T. Variationally optimized atomic orbitals for large-scale electronic structures. *Phys. Rev. B* **67**, 155108 (2003).
65. Perdew, J. P., Burke, K. & Ernzerhof, M. Generalized gradient approximation made simple. *Phys. Rev. Lett.* **77**, 3865–3868 (1996).